CrystEngComm

PAPER

View Article Online
View Journal | View Issue

Open Access Article. Published on 01 March 2016. Downloaded on 1/21/2026 11:25:34 PM.
This article is licensed under a Creative Commons Attribution 3.0 Unported Licence.

Cite this: *CrystEngComm*, 2016, **18**, 2532

Comparison of amorphous, pseudohexagonal and orthorhombic Nb_2O_5 for high-rate lithium ion insertion†

Shuang Li,[ab] Qian Xu,[c] Evan Uchaker,[b] Xi Cao[b] and Guozhong Cao*[b]

Received 23rd October 2015,
Accepted 1st March 2016

DOI: 10.1039/c5ce02069g

www.rsc.org/crystengcomm

Amorphous, pseudohexagonal and orthorhombic Nb_2O_5 nanoparticles were synthesized using a facile and green sol–gel process followed by thermal treatment at 450 °C, 600 °C and 800 °C for 3 h in air, respectively. The resulting materials have been subjected to a detailed experimental study and comparison of their structural, electrical and electrochemical properties. The experiments have demonstrated that the pseudohexagonal Nb_2O_5 (TT-Nb_2O_5) exhibited higher storage capacity, largely due to its high specific surface area and small crystallites, and better cycling performance than both amorphous Nb_2O_5 (a-Nb_2O_5) and orthorhombic Nb_2O_5 (T-Nb_2O_5); such experimental findings were found to be associated with and thus ascribed to the lower charge transfer resistance and higher lithium ion diffusion coefficient of TT-Nb_2O_5 than those of a-Nb_2O_5 and T-Nb_2O_5. This research contributes to a better fundamental understanding of the relationship between the crystal structure and the crystallinity and electrochemical properties, particularly Li-ion storage properties, and leads to a possible new advancement in the research field of lithium ion batteries and pseudocapacitors.

Introduction

Electrochemical energy storage devices have attracted considerable attention in powering future advanced communication equipment, portable electronics, electric vehicles and smart grids.[1–3] For electric vehicles (EVs), the current commercial lithium-ion batteries (LIBs) commonly using graphite as the anode cannot meet the stringent requirements of high power density, because of poor rate performance and especially safety concerns.[4] Thus, developing advanced electrode materials, which possess better safety characteristics and high rates, becomes imperative. There are several promising candidates including silicon and tin-based compounds being actively studied as anodic materials for the next generation of batteries as they offer high lithium-ion storage capacities;[5–8] however, they suffer from huge volume changes accompanied by lithium ion insertion and extraction.[9] Lithium titanate ($Li_4Ti_5O_{12}$) is another most noticeable anodic material under intensive study as it offers a high charge/discharge voltage of 1.55 V (*vs.* Li/Li^+) and very stable cyclic stability since there is a very small volume change during lithium ion insertion and extraction; however, its lithium ion storage capacity is 170 mA h g^{-1} theoretically.[10] Niobium pentoxide (Nb_2O_5) is another anodic material which attracts a lot of attention lately, due to its unique fast ion diffusion property during lithium ion intercalation and extraction, and most research are based on pseudocapacitors.[11] It has been reported that the high rate is attributed to the fact that lithium ion insertion and extraction is rate-limited by the capacitive effect, not by lithium ion diffusion through the electrode.[12] Compared to commercial graphite anodes, Nb_2O_5 exhibits a similar insertion/extraction voltage to $Li_4Ti_5O_{12}$, which is higher than the 1 V voltage (*vs.* Li/Li^+) of SEI formation and suppresses lithium dendrite deposition on the surface of the anode.[13] In addition, Nb_2O_5 has a good theoretical lithium-ion storage capacity of 200 mA h g^{-1},[14] which leads to a higher energy density and makes it a good candidate for niche applications.

Due to its attractive physical properties, Nb_2O_5 has been extensively studied and applied in various technical applications such as electrochemical pseudocapacitors,[11,12] gas sensors,[15] catalysts,[16] electrochromics[17] and solar cells.[17,18] The electrochemical properties of Nb_2O_5 were first investigated by Bard *et al.*, who demonstrated that Nb_2O_5 exhibits lithium-ion intercalation properties, which led to further research of Nb_2O_5 as an anode for lithium ion batteries.[19,20] In recent years, various nanostructures of Nb_2O_5 as electrodes for lithium ion batteries have been studied, such as nanotubes, nanowires, nanofibers and spherical nanoparticles.[14,21–24]

[a] *School of Materials Science and Metallurgy, Northeastern University, Shenyang 110819, PR China*
[b] *Department of Materials Science and Engineering, University of Washington, Seattle, Washington 98195, USA. E-mail: gzcao@u.washington.edu*
[c] *State Key Laboratory of Advanced Special Steel, Shanghai University, Shanghai 200072, PR China*

† Electronic supplementary information (ESI) available. See DOI: 10.1039/c5ce02069g

This journal is © The Royal Society of Chemistry 2016

Open Access Article. Published on 01 March 2016. Downloaded on 1/21/2026 11:25:34 PM.
This article is licensed under a Creative Commons Attribution 3.0 Unported Licence.

Some research studies revealed that Nb_2O_5–C composites and Ti- or Ta-substituted Nb_2O_5 possessed improved electrochemical properties.[25–27] The Li intercalation properties of other Nb-based oxides are summarized in a recent review paper.[28] Nb_2O_5 has many polymorphic forms, such as a-Nb_2O_5 (amorphous Nb_2O_5), TT-Nb_2O_5 (pseudohexagonal Nb_2O_5), T-Nb_2O_5 (orthorhombic Nb_2O_5) and M-Nb_2O_5 (monoclinic Nb_2O_5), which can be obtained mainly through controlled thermal treatment. The study on the transition and structures of TT-Nb_2O_5, T-Nb_2O_5 and M-Nb_2O_5 phases has been discussed in the literature.[29] In Kodama *et al.*'s work, several crystal forms of Nb_2O_5 and their intercalation process were discussed mainly using *in situ* XAFS-XRD.[30] A. Le Viet *et al.* reported that M-Nb_2O_5 exhibited the highest capacity compared with T-Nb_2O_5 and tetragonal Nb_2O_5; besides, heat-treated M-Nb_2O_5 (1100 °C) in argon shows a much enhanced discharge capacity of 192 mA h g^{-1} at a current density of 150 mA g^{-1}.[27] Recently, Kim *et al.* synthesized a-Nb_2O_5, TT-Nb_2O_5 and T-Nb_2O_5 using different methods and reported their rapid pseudocapacitive characteristics by drop casting Nb_2O_5 nanoscale powders onto steel foils as electrodes.[11] These research studies have clearly indicated that Nb_2O_5 polymorphs are very promising lithium ion storage materials. What's more, fast transport kinetics is another important advantage along with high power density for lithium ion batteries besides large capacity. Thus, more studies based on a detailed comparison of the structural, electrical and electrochemical properties of a-Nb_2O_5, TT-Nb_2O_5 and T-Nb_2O_5 phase materials applied in lithium-ion batteries becomes necessary.

This paper reports the synthesis of nanostructured Nb_2O_5 *via* a facile and green sol–gel process with forced hydrolysis and condensation and investigates the electrochemical properties of a-Nb_2O_5, TT-Nb_2O_5 and T-Nb_2O_5 nanoparticles, aimed at achieving a better fundamental understanding of the relationship between the electrochemical properties, in particular Li-ion storage properties, and the crystallinity and nanostructures. Specifically, we introduced NH_4OH and H_2O_2 into the precursor solution to catalyze and promote rapid hydrolysis and condensation reactions. The resulting Nb_2O_5 nanoparticles were amorphous in nature and the subsequent annealing at elevated temperatures converted the amorphous niobium pentoxide to the pseudohexagonal phase and orthorhombic crystals. Upon evaluation as anode materials for lithium-ion batteries, the three Nb_2O_5 phases all showed very stable cycling performance, and the TT-Nb_2O_5 nanoparticles showed higher lithium ion storage capacity than both amorphous Nb_2O_5 and T-Nb_2O_5. Compared with the results for T-Nb_2O_5 and M-Nb_2O_5 reported in the literature, the pseudohexagonal crystal has the advantage of low processing temperature which can save energy in materials processing.

Experimental method

Materials synthesis

a-Nb_2O_5, TT-Nb_2O_5 and T-Nb_2O_5 nanoparticles were synthesized *via* a facile sol–gel process followed by annealing in air at 450 °C, 600 °C and 800 °C, respectively. In a typical reaction, 1 g of $NbCl_5$ was dissolved in 2 ml of ethanol, and a clear yellow $NbCl_5$ EtOH solution was formed. A white precipitate was subsequently obtained from this solution by dropwise addition of 5% dilute ammonia, and the pH value was tuned at 7.[31] The precipitate was isolated from the solution and washed with deionized water four times by centrifugation at 6000 rpm. Then, 4 ml of 30 wt% aqueous hydrogen peroxide was added to the precipitate. The mixture was stirred for 5 minutes in an ice bath, and then a transparent yellow sol was obtained. This sol was dried in an oven at 70 °C for 24 hours and then a clear yellow xerogel was obtained. The xerogel was ground into white particles and then annealed under ambient atmosphere at 450 °C (a-Nb_2O_5), 600 °C (TT-Nb_2O_5) and 800 °C (T-Nb_2O_5) for 3 hours.

Materials characterization

The crystalline structure of the particles obtained was characterized by X-ray diffraction (XRD, D8 Bruker X-ray diffractometer with Cu-Kα radiation (λ = 1.5418 Å)) within the range of 10–70° (2θ). X-ray photoelectron spectroscopy (XPS) analysis was performed using a VG Multilab 2000 with Al Kα as the X-ray source. The accelerating voltage and current were 40 kV and 40 mA, respectively. Scanning electron microscopy (SEM, JEOL, JSM-7000F) and transmission electron microscopy (TEM, FEI, Tecnai G2 F20) were used to examine the morphology and microstructure of the as-prepared samples. Thermogravimetric analysis (TGA) was performed on a TG instrument (NETZSCH STA 409C). Nitrogen adsorption–desorption isotherms were measured using a Quantachrome NOVA 4200e system. Samples were degassed at 250 °C under vacuum overnight prior to measurements. The specific surface areas and micropore volumes were determined by multipoint Brunauer–Emmett–Teller (BET), *t*-method and Barrett–Joyner–Halenda (BJH) desorption analyses, respectively.

Electrochemical property measurement

The electrochemical performance of the Nb_2O_5 polymorphs was tested in coin-type cells, which were assembled using the as-prepared samples in an argon-filled glove-box (Innovative Technology, IL-2GB). The as-prepared active materials were mixed and ground with poly(vinylidene fluoride) (PVDF, Sigma-Aldrich) as a binder and Super P conductive carbon (TIMCAL Graphite & Carbon) as the conductive assistant materials at a respective weight ratio of 70 : 20 : 10 in an *N*-methyl-2-pyrrolidone (NMP, Alfa Aesar) solution. The as-prepared mixture was uniformly spread and pressed onto an aluminum foil and dried in a vacuum oven at 80 °C overnight for use as the working electrode. The mass of the active material is approximately 0.5 mg. A pure lithium foil was used as the counter and reference electrodes. A polypropylene membrane film (Celgard 2400) was used as the separator. 1 M $LiPF_6$ in ethylene carbonate (EC)/dimethyl carbonate (DMC) was used as the electrolyte. Galvanostatic charge/discharge measurements were performed in the voltage range of 1.2 to

Open Access Article. Published on 01 March 2016. Downloaded on 1/21/2026 11:25:34 PM.
This article is licensed under a Creative Commons Attribution 3.0 Unported Licence.

3.0 V (*vs.* Li/Li^+) under different current densities. Cyclic voltammetry (CV) was conducted on an electrochemical analyzer (CH Instruments, model 605C) in the voltage range of 1.2 to 3.0 V (*vs.* Li/Li^+) at a scan rate of 0.2 mV s^{-1}. Electrochemical impedance spectroscopy (EIS) studies were performed on a Solartron 1287A in conjunction with a Solartron 1260FRA/impedance analyzer with an amplitude of 5.0 mV in the frequency range from 100 kHz to 0.1 Hz. The half-cells were tested at various current rates based on the weight of the active material.

Results and discussion

When $NbCl_5$ was dissolved in absolute ethanol, the following reaction would occur, leading to the formation of niobium chloride ethoxide:[32]

$$NbCl_5 + xCH_3CH_2OH \rightarrow NbCl_{5-x}(CH_3CH_2O)_x + xHCl \quad (1)$$

Continuous stirring would allow the partial removal of HCl through evaporation, promoting reaction (1) further, and also the absorption of H_2O from air, resulting in partial hydrolysis:

$$NbCl_{5-x}(CH_3CH_2O)_x + yH_2O \rightarrow Nb(CH_3CH_2O, OH)_5 + (5-x)HCl + (y+x-5)HOCH_2CH_3 \quad (2)$$

When NH_4OH was subsequently added, it reacted with HCl, increased the pH value, and promoted the hydrolysis and condensation reactions of niobium alkoxide as a catalyst, and the white precipitate of $Nb(OH)_5$ was subsequently obtained:

$$NH_4OH + HCl \rightarrow NH_4Cl + H_2O \quad (3)$$

$$Nb(CH_3CH_2O, OH)_5 + 5H_2O \rightarrow Nb(OH)_5 + HOCH_2CH_3 \quad (4)$$

NH_4Cl is a white precipitate in ethanol.[32] However, in the present work, no NH_4Cl precipitate was observed, probably due to the low percentage of ethanol.

Collectively, the purpose of adding NH_4OH to the niobium oxide sol is to promote both the hydrolysis and condensation reactions, and it consequently resulted in a rapid nucleation process with a high density of nuclei of narrow size distribution. The addition of H_2O_2 dissolved the precipitate and turned the colour from ivory to yellow; upon drying in an oven at 70 °C, the release of the oxygen gas by-product benefits the nucleation process as well. The release and removal of oxygen gas bubbles from the sol helped homogenize the concentration and temperature of the sol so as to ensure a uniform size of the nanoparticles, and also prevented the possible formation of agglomerated nanoparticles. The SEM images shown in Fig. 4b and d have demonstrated the difference between the as-synthesized Nb_2O_5 nanoparticles synthesized with and without the addition of H_2O_2 through a sol–gel process under otherwise the same conditions. The Nb_2O_5 nanoparticles synthesized with the addition of H_2O_2 are smaller and are dispersed better, *i.e.*, less aggregated.

Through a thermal treatment process, different Nb_2O_5 polymorphs were formed using the above-mentioned method. The crystalline structure and crystallinity of the as-prepared materials annealed at different temperatures were examined by XRD, and the results are displayed in Fig. 1. The intensity and shape of the diffraction peaks vary greatly as the annealing temperature changes. The as-prepared Nb_2O_5 xerogel was amorphous. At the annealing temperature of 450 °C, the diffraction peaks are mild, and the pattern has a shape close to that of an amorphous crystal. This might be attributed to the fact that the particles could not change into crystals very well at this annealing temperature. When the annealing temperature is 600 °C, pseudohexagonal crystals of Nb_2O_5 (TT-Nb_2O_5) are formed. All the diffraction peaks are clear and in good agreement with those of TT-Nb_2O_5 (space group: *P*6/*mmm*, JCPDS: 28-317), though the intensity of the peaks is weak, the peaks are broad and the signal-to-noise ratio is low, which are all indicative of small crystal size and/or poor crystallinity. The average crystallite size of TT-Nb_2O_5 was calculated to be approximately 22.5 nm using the Scherrer equation. Between 600 °C and 800 °C, there is a crystal transition. When the annealing temperature is raised to 800 °C, the diffraction peaks are consistent with the peaks of orthorhombic Nb_2O_5 (T-Nb_2O_5, space group: *Pbam*, JCPDS: 30-0873). The average crystallite size was estimated to be ~113.3 nm using the Scherrer equation. The crystallites of the T-phase are significantly larger than those of TT-Nb_2O_5, as the annealing temperature is much higher. The high intensity and narrow width of the T-Nb_2O_5 peaks imply that it crystallized very well at the annealing temperature of 800 °C.

In order to study the crystalline water loss and the crystal transition during the annealing process, TGA was carried out in flowing air from 30 °C to 830 °C with a heating rate of 10 °C min^{-1} and the TGA curve of the pure Nb_2O_5 xerogel is shown in Fig. 2. From the TGA curve, we can see that the weight loss started with a mild curve from room temperature

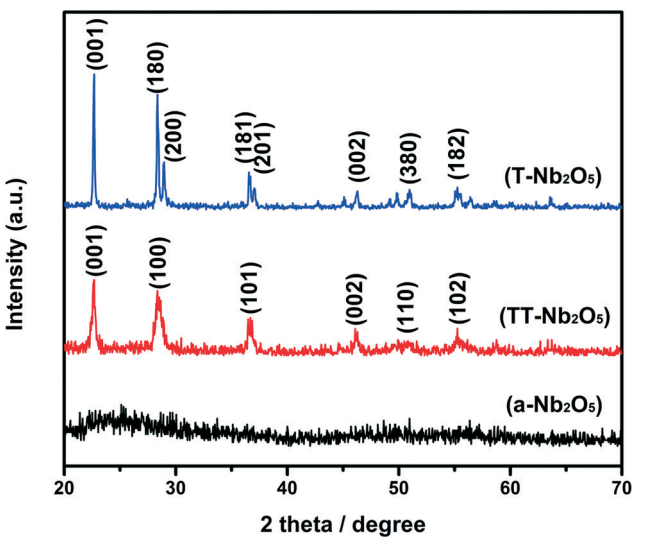

Fig. 1 XRD patterns of Nb_2O_5 polymorphs annealed in air for 3 hours at different temperatures: (a-Nb_2O_5): 450 °C; (TT-Nb_2O_5): 600 °C; (T-Nb_2O_5): 800 °C.

 This journal is © The Royal Society of Chemistry 2016

Open Access Article. Published on 01 March 2016. Downloaded on 1/21/2026 11:25:34 PM.
This article is licensed under a Creative Commons Attribution 3.0 Unported Licence.

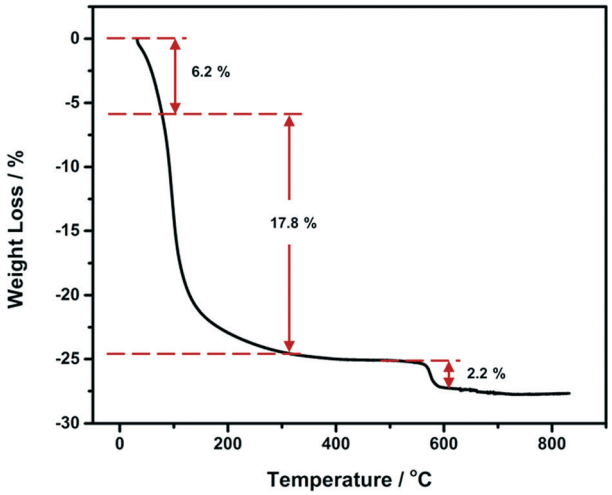

Fig. 2 TGA curve of the pure Nb_2O_5 xerogel from 30 °C to 830 °C at a rate of 10 °C min^{-1}.

to around 90 °C which is supposed to be the physically adsorbed water molecules. A large mass loss of about 20% from 90 to 300 °C mainly involves fragments of organic molecules (C_xH_y) and HCl, and it is attributed to the build-up of the inorganic amorphous network.[33] The lower mass loss of 2.2% at around 580 °C accompanying the crystallization process is due to a transformation from an uncharacterized niobium pentoxide hydrate, also known as niobic acid or columbic acid ($Nb_2O_5{\cdot}nH_2O$), gel to a Nb_2O_5 crystal (pseudo-hexagonal).[31] From 600 °C to 800 °C, the weight loss is less than 0.5%, which means that although the morphology variation is significant and the crystal structure changes from pseudohexagonal to orthorhombic, the weight loss is inconspicuous. This result agrees well with the works published in the literature.[17,24] In these works, no appreciable weight loss or crystallization peaks (from their differential thermal analysis results) were observed for the crystal structure change from pseudohexagonal to orthorhombic.

XPS analyses were carried out in the region of 0–800 eV to elucidate the chemical composition. Fig. 3 shows the typical XPS spectra taken from the niobium and oxygen regions of TT-Nb_2O_5. The binding energy scales of the spectra were calibrated by assigning the most intense C 1s peak a binding energy of 284.8 eV. Fig. 3a reveals that the sample contains the Nb, O and C elements. In Fig. 3b, the Nb 3d level binding energies of TT-Nb_2O_5 were 207.3 and 210.0 eV, which are attributed to the doublet Nb $3d_{5/2}$ and Nb $3d_{3/2}$ core levels of Nb^{5+}, respectively. These binding energies of Nb^{5+} ions are in close agreement with the values reported.[34,35] Fig. 3c shows the binding energies of the O 1s peaks. Among these peaks, the sharp one located at 529.6 eV and the low one located at 531.9 eV are assigned to O^{2-} in Nb-oxides and surface oxygen, respectively.[24] Another O 1s peak located at 530.7 eV could be the peak of C–O from some possible residual groups.

SEM and TEM were carried out to investigate the microstructure and morphology of the as-synthesized samples. As shown in Fig. 4a, a-Nb_2O_5 annealed at 450 °C has smaller particle size, better dispersion and higher porosity. From Fig. 4b, it can be clearly seen that the particles are formed homogeneously after being annealed at 600 °C for 3 h in air, and the TT-Nb_2O_5 particles have a narrow size distribution at around 20 nm. When the powders were annealed at 800 °C (Fig. 4c), larger-sized T-Nb_2O_5 particles of around 100 nm size were obtained. This means that the rise in temperature not only modified the crystalline phase but also increased the size. Fig. 4d presents the SEM image of the Nb_2O_5 particles without addition of hydrogen peroxide and annealed at 600 °C for 3 h in air. In this image, connections between particles can be found. By comparing Fig. 4b and d, it can be clearly seen that the particles in Fig. 4b have much better uniform dispersion, which also proved that the addition of H_2O_2 can improve the dispersity of Nb_2O_5 nanoparticles. The high-resolution TEM images provide more detailed structural information as seen in Fig. 5. Compared to a-Nb_2O_5 shown in Fig. 5a, the lattice fringes of the TT-Nb_2O_5 and T-Nb_2O_5 particles can be clearly observed in Fig. 5b and c, suggesting the presence of a well-defined crystal structure. The periodic lattice fringe spacings in Fig. 5b were found to be 0.32 and 0.25 nm corresponding to the interplanar spacings of the (100) and (101) planes, respectively, for pseudohexagonal Nb_2O_5 (JCPDS: 28-317); in Fig. 5c, the periodic lattice fringe spacings were 0.38 and 0.31 nm which agreed well with the interplanar spacings of the (001) and (180) planes. These results further corroborate the findings from XRD.

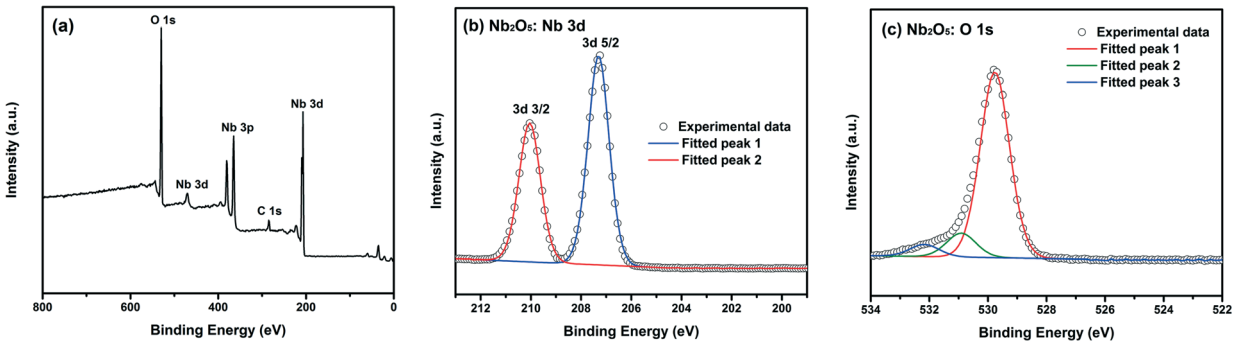

Fig. 3 XPS spectrum of (a) wide survey of TT-Nb_2O_5 nanoparticles, (b) the zone-in Nb 3d spectrum and (c) the zone-in O 1s spectrum.

Open Access Article. Published on 01 March 2016. Downloaded on 1/21/2026 11:25:34 PM.
This article is licensed under a Creative Commons Attribution 3.0 Unported Licence.

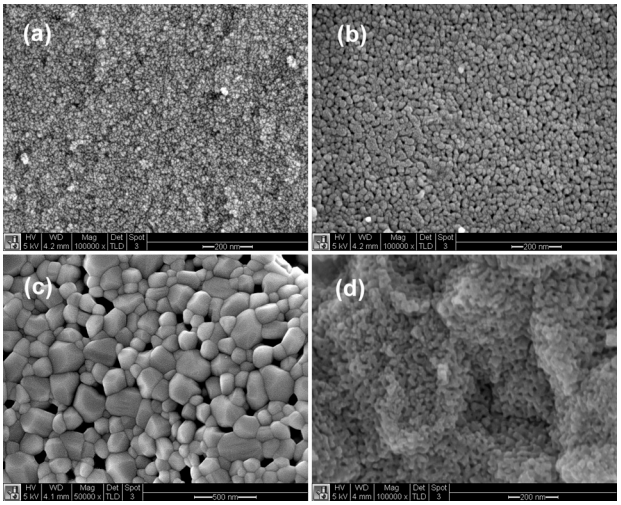

Fig. 4 SEM images of Nb_2O_5 particles (a) obtained from a-Nb_2O_5, (b) with H_2O_2 annealed at 600 °C, (c) with H_2O_2 annealed at 800 °C in air for 3 h and (d) without addition of H_2O_2 and annealed at 600 °C.

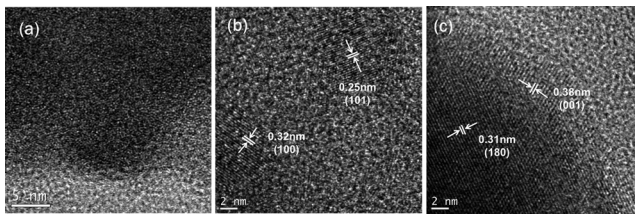

Fig. 5 High-resolution TEM images of (a) a-Nb_2O_5, (b) TT-Nb_2O_5 and (c) T-Nb_2O_5.

The presence of pores and the porous distribution of the Nb_2O_5 polymorphs were confirmed by the corresponding nitrogen sorption isotherms and Barrett–Joyner–Halenda (BJH) desorption analyses which are shown in Fig. 6. The results in Fig. 6a indicated that the pore size of a-Nb_2O_5 centrally distributed at 3.5 nm which was the only mesopore distribution can be found, and the Brunauer–Emmett–Teller (BET)-derived surface area was determined to be 129.6 $m^2\ g^{-1}$. Within the TT-Nb_2O_5 sample, the majority of the pores are around 15 nm (Fig. 6b) and exhibit a very narrow pore size distribution. The BET surface area of TT-Nb_2O_5 was 57.8 $m^2\ g^{-1}$, which is a reasonable value providing excellent channels and cavities for complete and homogeneous Li^+ diffusion and intercalation throughout the material.[36] For the T-Nb_2O_5 sample (Fig. 6c), no obvious pore size distribution was observed in our study, and the peaks of pore size distributions at 3.5 and 5 nm are very weak. The surface area of T-Nb_2O_5 turns out to be only 43.0 $m^2\ g^{-1}$, which is far lower than those of a-Nb_2O_5 and TT-Nb_2O_5.

In order to investigate the storage properties of the Nb_2O_5 polymorphs, CV, galvanostatic charge/discharge measurements and electrochemical impedance analysis have been performed. The CV curves of the first, second and fifth runs for the a-Nb_2O_5, TT-Nb_2O_5 and T-Nb_2O_5 samples collected at a scan rate of 0.2 mV s^{-1} in the voltage range of 1.2–3.0 V (*vs.* Li/Li^+) are shown in Fig. 7. The three Nb_2O_5 polymorphs all showed good reusability. For T-Nb_2O_5 (Fig. 7c), the current response of the cathodic sweep increases greatly below 2.1 V (*vs.* Li/Li^+), and two obvious reduction reactions located at 1.72 and 1.54 V correspond to the valence variation during the intercalation process. On the reverse sweep, an ambiguous broad peak at 1.82 V reveals that the continuous variation from Nb^{4+} back to Nb^{5+} takes place during the redox process.[30] The cathodic and anodic peaks of TT-Nb_2O_5 (Fig. 7b) are broad and located at 1.5 V and 1.85 V, respectively. In contrast, the CV peaks of the a-Nb_2O_5 material (Fig. 7a) are very obscure except for the first cycle which exhibits a small reduction peak at 2.0 V and a wide shift of the CV curve to the other cycles.

Fig. 8 displays the charge–discharge profiles of the Nb_2O_5 polymorphs for the first three cycles at a current rate of 10 mA g^{-1} in the voltage range of 1.2–3.0 V (*vs.* Li/Li^+). As shown in Fig. 8a, a-Nb_2O_5 exhibited an initial discharge capacity of 291 mA h g^{-1}, but it dropped to 150 mA h g^{-1}, nearly half of the first discharge capacity, after the second cycle. Similarly, TT-Nb_2O_5 and T-Nb_2O_5 showed a decrease in capacity following the first cycle; however, the proportion of reversible capacity in the second cycle is much larger than that for a-Nb_2O_5, at around 80% for both TT-Nb_2O_5 and T-Nb_2O_5. a-Nb_2O_5 exhibited the highest initial discharge capacity and the largest decay in the second cycle. This agrees well with the CV curves in Fig. 7a, which possess a wide shift between the first and second reduction curves, suggesting a large

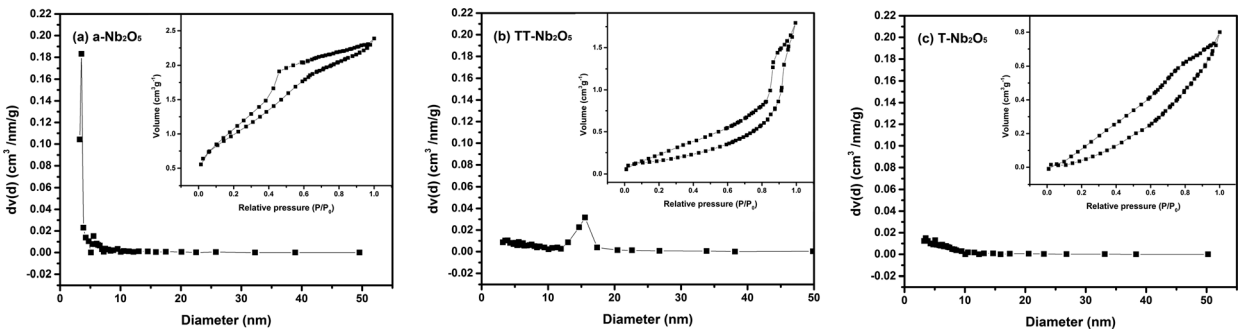

Fig. 6 BJH desorption pore size distribution for the as-synthesized Nb_2O_5 polymorphs: (a) a-Nb_2O_5, (b) TT-Nb_2O_5 and (c) T-Nb_2O_5 (inset: N_2 adsorption–desorption isotherm).

 This journal is © The Royal Society of Chemistry 2016

Open Access Article. Published on 01 March 2016. Downloaded on 1/21/2026 11:25:34 PM.
This article is licensed under a Creative Commons Attribution 3.0 Unported Licence.

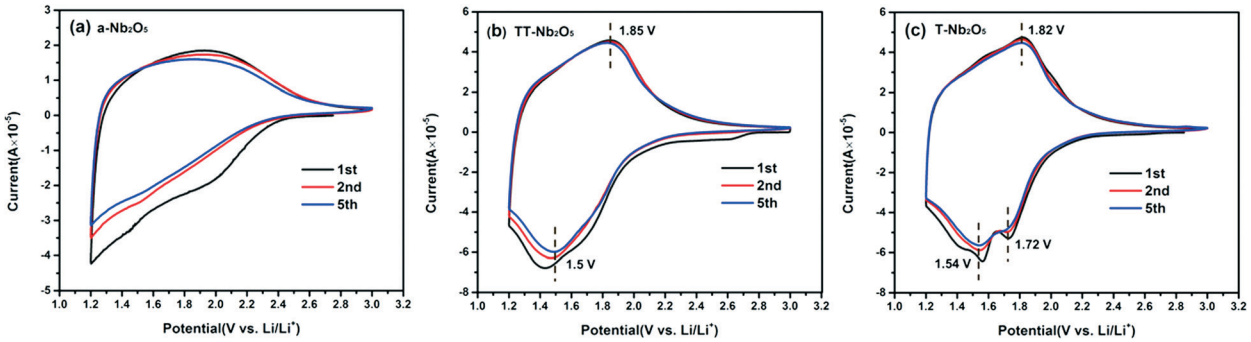

Fig. 7 CV curves of Nb_2O_5 polymorph electrode materials: (a) a-Nb_2O_5, (b) TT-Nb_2O_5 and (c) T-Nb_2O_5 measured in the voltage range of 1.2–3.0 V (*vs.* Li/Li^+) with a scan rate of 0.2 mV s^{-1}.

capacity decrease. In contrast, the CV curves for crystalline Nb_2O_5 (Fig. 7b and c) are more reversible between the first two cycles. In addition, from Fig. 7a, a mild reduction peak located at 2.0 V revealed that an irreversible chemical reaction with Li could exist.[37] On the other hand, from the TGA analysis in Fig. 2, a-Nb_2O_5 should involve the loss of 2.2% located at 580 °C in the form of hydroxyl groups (O–H), which could bring about an undesirable irreversible electrochemical reaction with Li in the initial cycle.[38,39] The existence of O–H in amorphous materials has been proven in previous reports, and it is also not detected in a fully crystallized material.[40] From the figures of TT-Nb_2O_5 and T-Nb_2O_5, curves of a similar shape can be found which have no plateaus, implying that the charge and discharge processes of the TT-Nb_2O_5 and T-Nb_2O_5 samples are very fast, which are in good agreement with the characteristics of pseudocapacitance.[12,41] Among the three samples, TT-Nb_2O_5 shows the highest reversible charge/discharge capacities of about 190 mA h g^{-1} which is much higher than the capacity of 110 mA h g^{-1} reported by Kodama *et al.*[30] Such a high capacity might be the result of a high specific surface area and the nanosized crystallites. For the larger-sized T-Nb_2O_5, the reversible charge/discharge capacities in the present study are similar to the results reported in the literature.[27] From here, we see that the difference is probably because of the fact that the nanoscale TT-Nb_2O_5 particles obtained by this sol–gel method can provide a larger surface area for Li^+ de/intercalation and thereby improve the capacity.[3] More capacities under different charge rates and stabilities are shown in Fig. 9.

The rate performance of the a-Nb_2O_5, TT-Nb_2O_5 and T-Nb_2O_5 samples at various charge–discharge rates is compared in Fig. 9. The charge–discharge curves show that all these three Nb_2O_5 polymorphs have very regular performance. No obvious fading can be found after 120 cycles. Among these samples, the TT-Nb_2O_5 electrode shows the highest capacity at each current rate. The discharge capacities measured in the voltage window from 1.2 V to 3 V are 191, 164, 146, 130, 122 and 114 mA h g^{-1} at the current densities of 50, 100, 200, 300, 400 and 500 mA g^{-1}, respectively. More importantly, when the current rate was reversed back to 100 mA g^{-1} after testing at the abovementioned different rates, the discharge capacity went back up to 172 mA h g^{-1} which is even higher than the initial discharge capacity at the same rate (164 mA h g^{-1}). This implies that the decline in capacity at high rates is limited. After 120 charge–discharge cycles, the TT-Nb_2O_5 electrode demonstrated a specific discharge capacity of 170 mA h g^{-1} at a current density of 100 mA g^{-1}, which is close to the capacity of the high-temperature phase, the pristine monoclinic phase, in a

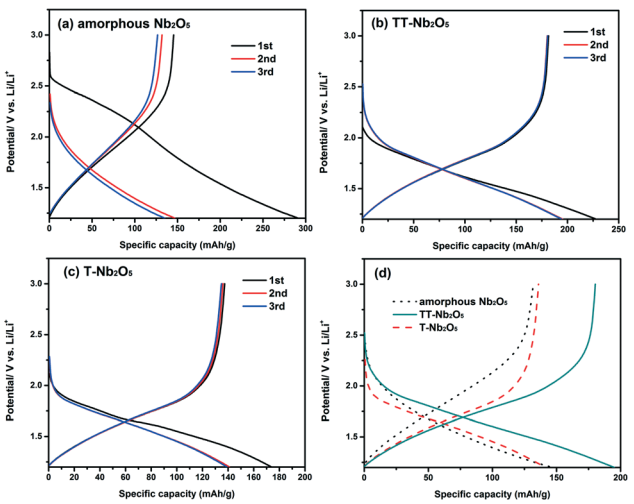

Fig. 8 First three discharge and charge curves of the samples at a current density of 10 mA g^{-1} in a half-cell: (a) a-Nb_2O_5, (b) TT-Nb_2O_5, (c) T-Nb_2O_5 and (d) a comparison of the second cycle curves of the three samples.

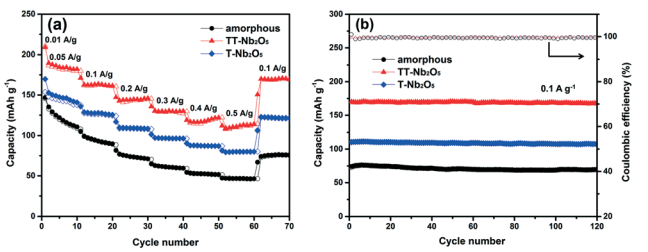

Fig. 9 (a) Rate capability of the Nb_2O_5 polymorphs at different current densities and (b) cycling performance of the Nb_2O_5 polymorphs at a current density of 100 mA g^{-1}.

Open Access Article. Published on 01 March 2016. Downloaded on 1/21/2026 11:25:34 PM.
This article is licensed under a Creative Commons Attribution 3.0 Unported Licence.

report.[27] Possessing relatively stable charge–discharge performance, the T-Nb_2O_5 electrode showed much lower capacities than the TT-Nb_2O_5 electrode at each current rate mentioned above, and its specific discharge capacity was stable at 110 mA h g^{-1} during 120 charge–discharge cycles. Apparent fading was observed during the first 20 cycles in the rate capability of the a-Nb_2O_5 electrode. What's more, the a-Nb_2O_5 electrode showed even lower capacities at different current rates; especially, when the current rate was 500 mA g^{-1}, the capacity fell to as low as 50 mA h g^{-1}. The intercalation reaction is sensitive to doping, preparation temperature and particle size which was also documented in TiO_2 as well as other systems.[42] It should be noted that research on other transition-metal oxides such as Fe_2O_3 and MnO_x showed that the amorphous phase possessed much enhanced performance compared to its crystalline counterpart.[37,43] The reason for these results has been explained to be their unique structures which are beneficial for lithium ion storage. Upon comparing the CV curves between the amorphous and crystalline phases, only small changes could be found such as slight shifts of peak location, peak intensity or/and peak width. However, the main CV curves between the amorphous and crystalline samples are very similar, which implies that, for these two materials, there are no significant mechanism differences in the lithiation process caused by changing the crystalline material into an amorphous one. In contrast, our CV results reveal that there are either some mechanism changes in the lithiation process or some capacity deficiency because the CV curve of a-Nb_2O_5 significantly changed with a lack of redox reaction peaks compared with that of crystalline Nb_2O_5. Those different lithiation mechanisms may explain the result that crystalline Nb_2O_5 showed better lithium ion storage properties than a-Nb_2O_5 in the present work.

For the sake of comparison of the electrochemical properties of M-Nb_2O_5, the Nb_2O_5 precursor was annealed at 1100 °C in air for 3 h and the resulting monoclinic phase was obtained as confirmed by the XRD patterns shown in Fig. S1a (ESI†). The electrochemical properties (shown in Fig. S1, ESI†) turned out to be in good agreement with those reported in the literature.[24] More specifically, the discharge–charge profiles showed a clear discharge plateau at a potential around 1.65 V, which is the same as that reported in the literature.[24] However, the CV curves were slightly different in appearance, which was likely due to the high scan rate used in the current study as compared with that in the literature (0.2 mV s^{-1} *vs.* 0.058 mV s^{-1}). The resulting M-Nb_2O_5 demonstrated a high reversible capacity of 185 mA h g^{-1} at a low rate of 10 mA g^{-1}. The capacity was found to be 120 mA h g^{-1} at a high rate of 100 mA g^{-1}. The M-Nb_2O_5 in the current investigation possessed a smaller capacity as compared to TT-Nb_2O_5.

To investigate the electrochemical kinetics of the Li^+ intercalation/deintercalation process within the Nb_2O_5 polymorphous electrode, EIS measurement was performed over a frequency range of 100 kHz to 0.1 Hz with the results shown in Fig. 10. The impedance data were recorded for fresh cells after 5 discharge–charge cycles at a current rate of 0.5 C. The voltage was 3.0 V under the charging status. As shown in the figure, the Nyquist plots of the a-Nb_2O_5, TT-Nb_2O_5 and T-Nb_2O_5 electrodes display a single semicircle in the high-frequency region and a straight line in the low-frequency range. The EIS was simulated through Z-view software using the equivalent circuit shown in the inset.[35,44,45] It consists of the solution resistance (R_s), charge transfer (R_{ct}) resistance, a constant phase element (CPE_1) and diffusional component Warburg impedance (Z_w). The semicircle at the high-frequency region is associated with the charge transfer resistance (R_{ct}).[46,47] The fitted R_{ct} values are 332.9 Ω, 261.5 Ω and 400.9 Ω for the a-Nb_2O_5, TT-Nb_2O_5 and T-Nb_2O_5 electrodes, respectively.

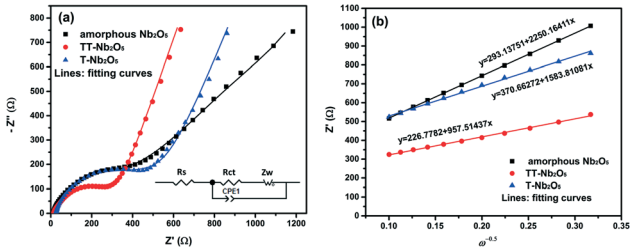

Fig. 10 (a) EIS plots of the Nb_2O_5 polymorphs at 25 °C and (b) the Z'–$\omega^{-0.5}$ plots in the low-frequency range.

With the lowest R_{ct} value, TT-Nb_2O_5 demonstrates better electrical conductivity, which can be a reason for its higher capacity and cycling performance. The straight line in the low-frequency range stands for the Warburg impedance.[48] The diffusion coefficient of lithium ions, D_{Li}, as one of the main kinetic factors in the rate-determining step of the intercalation process, can be calculated using several techniques, such as CV, EIS and the galvanostatic intermittent titration technique (GITT). These testing methods are based on their respective formula derived by using Fick's law and the Nernst equation. The differences mostly come from adopting different boundary conditions, initial conditions and numerical analysis methods. The CV technique can provide quantitative information on the electrode process, and the reversibility, stability and phase transformations during the intercalation and deintercalation reactions. The GITT is established to be a reliable technique for investigating the D_{Li} with highly resolved data for intercalation compounds of varying lithium content or potential. EIS is also a powerful technique for calculating the D_{Li} due to the fact that the low-frequency Warburg contribution of the impedance response is directly related to the lithium-ion diffusion process in an electrode material.[49] Slight differences in the diffusion coefficient may exist when different testing techniques were applied; however, D_{Li} obtained from the same technique can still be used to analyze and compare different systems and different electrode materials. The D_{Li} here was calculated from the plots in the low-frequency region. The equation for the calculation of D_{Li} values by EIS can be expressed as follows:[50–52]

 This journal is © The Royal Society of Chemistry 2016

Open Access Article. Published on 01 March 2016. Downloaded on 1/21/2026 11:25:34 PM.
This article is licensed under a Creative Commons Attribution 3.0 Unported Licence.

$$Z' = R_b + R_{ct} + \sigma\omega^{-0.5} \quad (5)$$

$$D_{Li} = \frac{(RT)^2}{2(An^2F^2C_{Li}\sigma)^2} \quad (6)$$

where T is the absolute temperature, R is the gas constant, n is the number of electrons per molecule during oxidization, A is the surface area, F is Faraday's constant, C_{Li} is the concentration of lithium ions, ω is the angular frequency, and σ is the Warburg factor, which has a relationship with Z'. The Z'–$\omega^{-0.5}$ plots are presented in Fig. 10b.

Based on the fitting linear equation in Fig. 10b, the Li-ion diffusion coefficients of a-Nb_2O_5, TT-Nb_2O_5 and T-Nb_2O_5 were calculated and the results are 1.39×10^{-21} cm^2 s^{-1}, 3.86×10^{-20} cm^2 s^{-1} and 2.56×10^{-20} cm^2 s^{-1}, respectively. The lower surface film and charge transfer resistance, higher Li-ion diffusion coefficient and electrical conductivity of the TT-Nb_2O_5 electrode lead to its superior rate capabilities and other electrochemical properties. Table 1 presents a summary of BET and EIS data of the three Nb_2O_5 polymorphs. In general, a larger surface area provides more reaction sites and shorter diffusion paths for ionic transport and electronic conduction, leading to a higher power density.[53] In this work, the crystallinity and crystal structure exhibit an obvious influence on the electrical conductivity as well as the ionic diffusivity. The surface area of a-Nb_2O_5 is twice as large as that of TT-Nb_2O_5; however, its resistance is lower than that of TT-Nb_2O_5. This means that during the process of crystal phase transition between the amorphous and TT phases, better crystallinity significantly reduced the value of resistance. In general, better crystallinity means more ordered arrangement of ions and fewer defects, which collectively offer more ordered passage for charge and mass transport, leading to fast diffusion and high conductivity (low resistance). During the transformation from the amorphous to TT phase, the crystals tend to be perfect. When the crystal phase transformed from the TT phase to the T phase, although the crystallinity improved to some extent, the particle size became larger, too. A larger particle size brings about long diffusion paths for ionic transport which can be a reason for high resistance.

Conclusions

a-Nb_2O_5, TT-Nb_2O_5 and T-Nb_2O_5 nanoparticles were synthesized using a facile and environmentally benign sol–gel process followed by thermal treatment. The size of the TT-Nb_2O_5 particles is around 20 nm, which is much smaller than that of T-Nb_2O_5 which is around 100 nm. The Nb_2O_5 nanoparticles synthesized with the addition of H_2O_2 are smaller and are dispersed better. Upon evaluation as anode materials for lithium-ion batteries, the a-Nb_2O_5, TT-Nb_2O_5 and T-Nb_2O_5 electrodes demonstrated specific discharge capacities of 149 mA h g^{-1}, 191 mA h g^{-1} and 152 mA h g^{-1}, respectively, at a current density of 50 mA g^{-1}. The large capacity of TT-Nb_2O_5 is most likely attributable to its large specific surface area. All these three Nb_2O_5 polymorphs have very stable cyclic stability within 120 cycles at a current density of 100 mA g^{-1}. In addition to its large capacity, TT-Nb_2O_5 possesses lower charge transfer resistance, a higher lithium ion diffusion coefficient and better electrical conductivity than both a-Nb_2O_5 and T-Nb_2O_5, which might be ascribed to its favourable crystal structure.

Table 1 Summary of BET and EIS results of Nb_2O_5 polymorphs

Samples	Specific surface area, m^2 g^{-1}	Pore size, nm	R_s, Ω	R_{ct}, Ω	Diffusion coefficients, cm^2 s^{-1}
a-Nb_2O_5	130	3.5	12.09	332.9	1.39×10^{-21}
TT-Nb_2O_5	58	15	12.38	261.5	3.86×10^{-20}
T-Nb_2O_5	43	—	12.75	400.9	2.56×10^{-20}

Acknowledgements

Shuang Li would like to acknowledge the financial support in the form of a scholarship from the China Scholarship Council (CSC) for her Ph.D. study at the University of Washington. This research was also financially supported in part by the National Science Foundation (NSF, DMR-1505902).

Notes and references

1 M. Armand and J. M. Tarascon, *Nature*, 2008, **451**, 652–657.
2 C. Liu, F. Li, L.-P. Ma and H.-M. Cheng, *Adv. Mater.*, 2010, **22**, E28–E62.
3 Q. Zhang, E. Uchaker, S. L. Candelaria and G. Cao, *Chem. Soc. Rev.*, 2013, **42**, 3127–3171.
4 M. M. Rahman, R. A. Rani, A. Z. Sadek, A. S. Zoolfakar, M. R. Field, T. Ramireddy, K. Kalantar-zadeh and Y. Chen, *J. Mater. Chem. A*, 2013, **1**, 11019–11025.
5 A. Magasinski, P. Dixon, B. Hertzberg, A. Kvit, J. Ayala and G. Yushin, *Nat. Mater.*, 2010, **9**, 353–358.
6 S.-H. Ng, J. Wang, D. Wexler, K. Konstantinov, Z.-P. Guo and H.-K. Liu, *Angew. Chem., Int. Ed.*, 2006, **45**, 6896–6899.
7 L.-F. Cui, Y. Yang, C.-M. Hsu and Y. Cui, *Nano Lett.*, 2009, **9**, 3370–3374.
8 J. Fan, T. Wang, C. Yu, B. Tu, Z. Jiang and D. Zhao, *Adv. Mater.*, 2004, **16**, 1432–1436.
9 S. D. Beattie, D. Larcher, M. Morcrette, B. Simon and J.-M. Tarascon, *J. Electrochem. Soc.*, 2008, **155**, A158–A163.
10 M. R. Jo, K. M. Nam, Y. Lee, K. Song, J. T. Park and Y.-M. Kang, *Chem. Comm.*, 2011, **47**, 11474–11476.
11 J. W. Kim, V. Augustyn and B. Dunn, *Adv. Energy Mater.*, 2012, **2**, 141–148.
12 A. Veronica, C. Jérémy, A. L. Michael, K. Jong Woung, T. Pierre-Louis, H. T. Sarah, D. A. Héctor, S. Patrice and D. Bruce, *Nat. Mater.*, 2013, **12**, 518–522.
13 L. Shen, B. Ding, P. Nie, G. Cao and X. Zhang, *Adv. Energy Mater.*, 2013, **3**, 1484–1489.
14 M. Wei, Z.-M. Qi, M. Ichihara and H. Zhou, *Acta Mater.*, 2008, **56**, 2488–2494.

Open Access Article. Published on 01 March 2016. Downloaded on 1/21/2026 11:25:34 PM.
This article is licensed under a Creative Commons Attribution 3.0 Unported Licence.

15 R. A. Rani, A. S. Zoolfakar, J. Z. Ou, M. R. Field, M. Austin and K. Kalantar-zadeh, *Sens. Actuators, B*, 2013, **176**, 149–156.
16 D. Prasetyoko, Z. Ramli, S. Endud and H. Nur, *Mater. Chem. Phys.*, 2005, **93**, 443–449.
17 M. A. Aegerter, *Sol. Energy Mater. Sol. Cells*, 2001, **68**, 401–422.
18 A. Le Viet, R. Jose, M. Reddy, B. Chowdari and S. Ramakrishna, *J. Phys. Chem. C*, 2010, **114**, 21795–21800.
19 B. Reichman and A. J. Bard, *J. Electrochem. Soc.*, 1980, **127**, 241–242.
20 B. Reichman and A. J. Bard, *J. Electrochem. Soc.*, 1981, **128**, 344–346.
21 C. Yan and D. Xue, *Adv. Mater.*, 2008, **20**, 1055–1058.
22 M. V. Reddy, R. Jose, A. Le Viet, K. I. Ozoemena, B. V. R. Chowdari and S. Ramakrishna, *Electrochim. Acta*, 2014, **128**, 198–202.
23 M. Sasidharan, N. Gunawardhana, M. Yoshio and K. Nakashima, *Mater. Res. Bull.*, 2012, **47**, 2161–2164.
24 A. L. Viet, M. V. Reddy, R. Jose, B. V. R. Chowdari and S. Ramakrishna, *J. Phys. Chem. C*, 2009, **114**, 664–671.
25 B. Guo, X. Yu, X.-G. Sun, M. Chi, Z.-A. Qiao, J. Liu, Y.-S. Hu, X.-Q. Yang, J. B. Goodenough and S. Dai, *Energy Environ. Sci.*, 2014, **7**, 2220–2226.
26 G. Li, X. Wang and X. Ma, *J. Energy Chem.*, 2013, **22**, 357–362.
27 A. Le Viet, M. Reddy, R. Jose, B. Chowdari and S. Ramakrishna, *Electrochim. Acta*, 2011, **56**, 1518–1528.
28 M. Reddy, G. Subba Rao and B. Chowdari, *Chem. Rev.*, 2013, **113**, 5364–5457.
29 I. Nowak and M. Ziolek, *Chem. Rev.*, 1999, **99**, 3603–3624.
30 R. Kodama, Y. Terada, I. Nakai, S. Komaba and N. Kumagai, *J. Electrochem. Soc.*, 2006, **153**, A583–A588.
31 N. Uekawa, T. Kudo, F. Mori, Y. J. Wu and K. Kakegawa, *J. Colloid Interface Sci.*, 2003, **264**, 378–384.
32 C. J. Brinker and G. W. Scherer, *Sol–gel science: the physics and chemistry of sol–gel processing*, Academic Press, 2013.
33 M. Schmitt and M. A. Aegerter, *Electrochim. Acta*, 2001, **46**, 2105–2111.
34 N. Özer, M. D. Rubin and C. M. Lampert, *Sol. Energy Mater. Sol. Cells*, 1996, **40**, 285–296.
35 S.-Q. Guo, X. Zhang, Z. Zhou, G.-D. Gao and L. Liu, *J. Mater. Chem. A*, 2014, **2**, 9236–9243.
36 E. Uchaker, M. Gu, N. Zhou, Y. Li, C. Wang and G. Cao, *Small*, 2013, **9**, 3880–3886.
37 J. Guo, Q. Liu, C. Wang and M. R. Zachariah, *Adv. Funct. Mater.*, 2012, **22**, 803–811.
38 B. Xu, D. Qian, Z. Wang and Y. S. Meng, *Mater. Sci. Eng., R*, 2012, **73**, 51–65.
39 A. Kraytsberg and Y. Ein-Eli, *Adv. Energy Mater.*, 2012, **2**, 922–939.
40 E. Uchaker, Y. Z. Zheng, S. Li, S. L. Candelaria, S. Hu and G. Z. Cao, *J. Mater. Chem. A*, 2014, **2**, 18208–18214.
41 V. Augustyn, P. Simon and B. Dunn, *Energy Environ. Sci.*, 2014, **7**, 1597–1614.
42 C. T. Cherian, M. Reddy, T. Magdaleno, C.-H. Sow, K. Ramanujachary, G. S. Rao and B. Chowdari, *CrystEngComm*, 2012, **14**, 978–986.
43 Y. Jiang, D. Zhang, Y. Li, T. Yuan, N. Bahlawane, C. Liang, W. Sun, Y. Lu and M. Yan, *Nano Energy*, 2014, **4**, 23–30.
44 P. Nithyadharseni, M. Reddy, B. Nalini, M. Kalpana and B. Chowdari, *Electrochim. Acta*, 2015, **161**, 261–268.
45 B. Das, M. Reddy, C. Krishnamoorthi, S. Tripathy, R. Mahendiran, G. S. Rao and B. Chowdari, *Electrochim. Acta*, 2009, **54**, 3360–3373.
46 S. Hu, F. Yin, E. Uchaker, W. Chen, M. Zhang, J. Zhou, Y. Qi and G. Cao, *J. Phys. Chem. C*, 2014, **118**, 24890–24897.
47 M. Umeda, K. Dokko, Y. Fujita, M. Mohamedi, I. Uchida and J. R. Selman, *Electrochim. Acta*, 2001, **47**, 885–890.
48 S. S. Zhang, K. Xu and T. R. Jow, *Electrochim. Acta*, 2004, **49**, 1057–1061.
49 X. Rui, N. Ding, J. Liu, C. Li and C. Chen, *Electrochim. Acta*, 2010, **55**, 2384–2390.
50 Y.-F. Deng, S.-X. Zhao, Y.-H. Xu and C.-W. Nan, *J. Mater. Chem. A*, 2014, **2**, 18889–18897.
51 Q. Cao, H. P. Zhang, G. J. Wang, Q. Xia, Y. P. Wu and H. Q. Wu, *Electrochem. Commun.*, 2007, **9**, 1228–1232.
52 H. Song, Y. Liu, C. Zhang, C. Liu and G. Cao, *J. Mater. Chem. A*, 2015, **3**, 3547–3558.
53 G. Cao, *Synthesis, Properties and Applications*, World Scientific, 2004.

 This journal is © The Royal Society of Chemistry 2016